Northumbria Research Link

1   **Twice-milled magnetic biochar: a recyclable material for efficient removal of**

2   **methylene blue from wastewater**

3

4   *Nina Yan[a], Biao Hu[a], Zhiyu Zheng[a], Haiying Lu[b,c], Jingwen Chen[a], Xiaomei Zhang[a],*

5   *Xizhi Jiang[a], Yonghong Wu[d], Jan Dolfing[e], Lei Xu[a*]*

6

7   *[a] Institute of Agricultural Facilities and Equipment, Jiangsu Academy of Agricultural*

8   *Sciences, Engineering Technology Research Center of Biomass Composites and*

9   *Addictive Manufacturing, Jiangsu Province, Nanjing 210014, Jiangsu, P. R. China*

10   *[b] Co-Innovation Center for the Sustainable Forestry in Southern China, College of*

11   *Biology and the Environment, Nanjing Forestry University, Nanjing 210037, Jiangsu,*

12   *P. R. China*

13   *[c] National Positioning Observation Station of Hung-tse Lake Wetland Ecosystem in*

14   *Jiangsu Province, Hongze 223100, Jiangsu, P. R. China*

15   *[d] State Key Laboratory of Soil and Sustainable Agriculture, Institute of Soil Science,*

16   *Chinese Academy of Sciences, Nanjing 210008, Jiangsu, P. R. China*

17   *[e] Faculty Energy and Environment, Northumbria University, Newcastle-upon-Tyne,*

18   *NE1 8QH, UK*

19

20   *[*] Corresponding Authors*

21   *E-mail: xulei@jaas.ac.cn (Lei Xu)*

Abstract

22

23   Although magnetic modification has potential for preparing recyclable biochar, the

24   traditional preparation methods of loading magnetic materials on biochar will probably

25   lead to pore blockage and consequently remarkable adsorption recession. Herein, a

26   preparation method was developed in which ball milled biochar was loaded with

27   ultrafine magnetite and then milled for a second time, thus generating a magnetic,

28   recyclable biochar with minimal pore blockage. The deposits of magnetite did not

29   significantly wrap the biochar, although a decreased sorption performance was still

30   detectable. Benefitting from the extra milling step, surface functional groups and

31   specific surface areas of the adsorbents were largely restored, thus leading to a 93.8%

32   recovery adsorption of 84.6±2.5 mg/L on methylene blue. Meanwhile, the recyclability

33   of the material was not affected. The adsorption was driven by multiple interactions.

34   These twice-milled magnetic biochar is quite outstanding for sustainable removal of

35   aqueous contaminants with its recyclability and high sorption efficiency.

36   **Keywords:** Biochar, Magnetic, Adsorption, Methylene blue, Ball milling

37

1. Introduction

Research on magnetic biochar for aqueous contaminant adsorption has flourished in recent years due to its potential for adsorbent separation and recyclability after use (Huang et al., 2022; El-Naggar et al., 2022). A wide range of Fe-modified biochar composites has been developed through liquid-phase chemical reactions or physical mechanical treatment of biochar with different iron sources (Wang et al., 2020a; Shan et al., 2016).

With these chemical methods, colloidal and nano-sized oxyhydroxides with particle size from ~100 to 600 nm tend to precipitate upon porous micron-level carbon platform of the biochar (Alchouron et al., 2021). Even though the amounts of the magnetic materials can be regulated by the preparation conditions, depressed adsorption performance caused by plugged pores on the adsorbent has been observed repeatedly (Tang et al., 2022). Consequently, significantly reduced adsorption capacity for heavy metals as well as organics after deposition of magnetite on biochar has been observed due to a decrease in the specific surface areas (SSA) of the adsorbent (Li et al., 2019; Son et al., 2018).

Physicomechanical treatment, especially ball milling, is considered an effective and economical alternative technique to promote the adsorption efficiency and shorten equilibrium time (Li et al., 2020a; Qu et al., 2022). This high-energy mechanical technology has been applied for the preparation of magnetic biochar in recent years as it can lower the hydrodynamic radius of the biochar, increase the SSA and pore volume (PV) and promote the generation of O-containing functional groups (Li et al., 2020b).

60 Thus, the number of adsorption sites was greatly increased. The as-fabricated magnetic

61 biochar has the great potential to remove various aqueous contaminants including Cr(VI)

62 (Wang et al., 2020a), pharmaceutical (Shan et al., 2016) and methylene blue (Li et al.,

63 2020b). However, it is difficult to optimize the functional characteristics of the magnetic

64 biochar with ball milling. Furthermore, the blocking of the pores is also observed in

65 ball milled magnetic biochar – just as it was in magnetic biochar prepared via chemical

66 methods – again resulting in a dramatically decreased SSA and adsorption capacity. For

67 example, SSA and PV of ball milled Fe^0-biochar were much smaller than SSA and PV

68 of ball milled biochar (Wang et al., 2020a). A decrease in SSA and adsorption capacity

69 was also reported by Li, who used adsorbent weight as base parameter (Li et al., 2020b).

70 To endow the biochar-based adsorbents with both excellent sorption and re-use

71 characteristics, an optimized magnetic biochar was developed in this work by

72 impregnating ball-milled biochar with magnetite followed by an extra ball milling step

73 to counteract the reduction in adsorption invariably caused by magnetite loading. The

74 comparison between traditional magnetic biochar and this work was illustrated in

75 Scheme 1. The physico-chemical properties of the adsorbents with step-by-step

76 treatment were examined carefully. The adsorption performance of the adsorbents was

77 assessed with a typical cationic toxic organic dye, methylene blue (MB). The adsorption

78 mechanism of the resultant adsorbents was also discussed and the reusability of the

79 adsorbents was evaluated.

80 **2. Material and methods**

81 **2.1 Materials**

82   The corn stalk powder was obtained from local suppliers. Triethylene glycol (TREG)

83   of analytical grade and iron (III) acetylacetonate (Fe(acac)$_3$, 98%) were provided by

84   Macklin (Shanghai, China). Ethyl acetate and ethanol of analytical grade were supplied

85   by Sinopharm Chemical Reagent Co., Ltd. MB ($\geq$98.5%) is provided by Nanjing

86   Chemical Reagent Co., LTD. All chemicals were used without further purification.

87   Deionized water was applied in all experiments.

88   **2.2 Magnetite loading on ball-milled biochar**

89   The preparation process is outlined in Scheme 1. The powder of corn stalks was first

90   pyrolyzed at 450 °C and ball milled under various conditions. The best ball milled

91   biochar was selected (see results section for details) and utilized as a platform for

92   magnetite loading with the polyol process (Cai and Wan, 2007). Magnetite-loaded

93   biochar (MmBCs) was finally obtained by vacuum-drying the residue at 60 °C for 24

94   h, followed by grinding. Different ratios of Fe(acac)$_3$ and ball milled biochar were

95   applied and the corresponding samples were labeled as MmBC-X according to the

96   respective ratio of X used. Magnetite nanoparticles were also prepared without biochar.

97   **2.3 The second ball milling process**

98   To recover the adsorption performance of MmBCs, which had deteriorated relative

99   to that of the original ball milled biochar (see results section for details), a second ball

100   milling step was applied. MmBC-0.6 (1.0 g) was placed in the zirconia jar and grinded

101   for 1 h at speeds of 100, 200, 300 or 400 rpm. The as-obtained samples were named

102   MmBC-BM100, MmBC-BM200, MmBC-BM300 and MmBC-BM400, respectively.

103   To allow comparisons with traditionally ball milled magnetic biochar, two pathways

104   were adopted for preparing the samples. In the 1st pathway, as-washed corn straw

105   powders (2 g) were placed in $FeCl_3$ solution (200 mL) with different concentrations and

106   stirred magnetically for 24 h. The impregnated biomass was calcined at 450 °C for 5 h

107   under nitrogen environment and ball-milled at 300 rpm for 5 h. The resultant magnetic

108   biochar was labeled as i-MBC-X (X is the concentration of $FeCl_3$ solution). In the 2nd

109   pathway, untreated corn straw-derived biochar was selected as a substrate to be

110   prepared by the same polyol process. The sample was further ball-milled at 300 rpm for

111   5 h and labeled as MBC-X where X represents the ratio between $Fe(acac)_3$ and biochar.

112   **2.4 Characterizations**

113   Boehm titration was used to quantify the surface acidic functional groups of different

114   samples (Boehm, 1994). X-ray diffraction (XRD, D2 Phaser, Bruker, Germany) data

115   were obtained with a wide-angle diffractometer with Cu Kα radiation (λ= 1.5418 Å) at

116   a generator voltage of 30 kV and current of 10 mA. Nitrogen adsorption-desorption

117   isotherms were determined with a Gemini VII 2390 Analyzer at 77 K (Micrometrics

118   Instrument Corp.) with the volumetric method. The SSA was calculated using the

119   Brunauer-Emmett-Teller (BET) method (Dollimore et al., 1976) in the relative pressure

120   range of 0.05-0.25. PV was estimated from the nitrogen adsorption isotherm at a

121   relative pressure P/P0=0.30. Magnetic characteristics were tested using a magnetometer

122   (MPMS XL-7, Quantum Design, USA) with versalab system at room temperature. The

123   magnetic field swept back and forth between -20,000 and 20,000 Oe. Other

124   characterizations were carried out followed with the previous work (Zheng et al., 2021).

2.5 MB adsorption experiments

Batch experiments were carried out to evaluate the MB adsorption performance of various adsorbents. Designated adsorbent (10 mg) was added into 50 mL of 20 mg L^{-1} MB solution and placed in a shaker (THZ-82) at 25±1 °C for 24 h to achieve adsorption equilibrium. After that, the mixture was filtered through a nylon filter with a pore size of 0.22 μm. The concentration was determined by UV absorbance at a wavelength of 665 nm with a UV-*vis* absorption spectrophotometer (NanoDrop ONE^{C}, Thermo). The removal capacity (q_e, mg g^{-1}) was calculated according to the concentrations (Li et al., 2020b). The kinetics and isotherms of MB adsorption were determined with the same procedure. The thermodynamic parameters and the corresponding models for sorption were also calculated. All experiments were performed in triplicate without adjusting solution pH except for those where the effect of pH on adsorption was quantified.

2.6 Desorption and regeneration

The reusability of MmBC-BM400 was evaluated by testing the regeneration and re-adsorption of MB for four cycles. Before each cycle, the sorbent (0.2 g L^{-1}) was added to MB solution (20 mg L^{-1}) for 24 h. After equilibrium adsorption, the exhausted sorbent was separated and collected by a magnet. The adsorbent was further regenerated with ethanol several times until the supernatant became colorless and transparent.

3. Results and discussion

3.1 Regulated preparation of magnetic biochar

To allow individual optimization of biochar and magnetite separately, a combination of physical and chemical routes was adopted. Biochar was first physically sheared by

147 ball milling at different speeds for different durations. As the effect of the milling

148 condition on the physicochemical properties of biochar have been presented and

149 discussed comprehensively in previous works (Lyu et al., 2018; Xiang et al., 2020a),

150 the detailed results of these preparation methods are presented (see supplementary

151 materials). Based on the relatively high SSA of 174.1 m^2 g^{-1} and PV of 40.0 cm^3 g^{-1} as

152 well as the abundance of O-containing functional groups (Table 1), the biochar milled

153 at 300 rpm for 5 h was selected as the platform for subsequent magnetite introduction.

154 This material had a saturated MB adsorption of 90.2 ± 4.1 mg g^{-1}.

155 Next, various mass ratios of Fe precursor to ball milled biochar were applied in

156 liquid-phase chemical reactions for magnetic biochar preparation. XRD patterns (see

157 supplementary materials) confirmed the successful synthesis of the magnetite with the

158 ball-milled biochar as they matched well with the standard XRD data (PDF number 01-

159 s019-0629) (Cai and Wan, 2007). Characteristic peaks strengthened while the peak

160 indexed as (0 0 2) plane of graphite structure in biochar at 26.5° weakened with the

161 ratio (Yamaguchi et al., 2016), implying an increased number of anchored magnetic

162 nanoparticles. The introduction of the magnetite did not influence the dispersion of the

163 adsorbent, but enhanced the superparamagnetic behaviors of MmBCs with ratios (see

164 supplementary materials). Considering that the ball-milled biochar itself is

165 nonmagnetic, the newly-acquired properties should be the result of the presence of

166 anchored magnetite, which is pivotal for adsorbent collection, separation and

167 reutilization with a magnet (Cao et al., 2019).

168   The microscopic morphologies of the ball-milled biochar before and after magnetite

169   preparation with the ratio of 0.6 were monitored in detail. Compared with the pristine

170   ball-milled biochar, some small particles were observed on MmBC-0.6, leading to a

171   much rougher surface. These closely-bonded particles are most likely to be the

172   introduced magnetite, which was confirmed by the TEM images (see supplementary

173   materials). The average size of the magnetic biochar with different ratios of precursors

174   are also listed (see supplementary materials). Magnetite obtained without ball milled

175   biochar was ~16.5 nm in size and this decreased to ~9.2 nm (revealed by the TEM

176   image) when generated in the presence of the carbonous materials. These ultrafine

177   magnetic particles were clumping together and loading on the ball milled biochar in

178   clusters, which results in an increased size of the adsorbents within 67.2 nm. The

179   adsorbent size, however, has no obvious relationship with the concentration of the

180   precursors.

181   The surface functional groups of ball milled biochar and MmBCs were also examined

182   by FT-IR. A new peak centering at ~575 cm^{-1} was only observed with MmBCs, which

183   corresponds to the tensile vibration peak of Fe-O (see supplementary materials) (Zhang

184   et al., 2020). However, the peaks of aromatic C=C (the aromatic C-C bond, or COO^{-})

185   stretching vibration at ~1585 cm^{-1} (Li et al., 2018), and stretching vibrations of –OH

186   centering around 3527 cm^{-1} (Zheng et al., 2021) declined with the appearance of

187   magnetite. The results of Boehm's titration quantitatively confirmed the significant

188   decrease of these functional groups from 0.598 to 0.271 mmol g^{-1} after magnetite

189   deposition at a ratio of 0.6 (Table 1), which is a 2.2-fold reduction. Meanwhile, carboxyl

190 and phenolic groups are making substantial contributions to the decrease. This is

191 reasonable as the magnetite itself has a relative insufficient number of carboxyl and

192 phenolic hydroxyl groups (Table 1). Furthermore, the functional groups on ball milled

193 biochar may be bonded or wrapped by magnetite. However, only a ~4 mV raise of zeta

194 potentials of MmBCs was observed (see supplementary materials), indicating that the

195 magnetite was only randomly scattered on rather than completely covering the surface

196 of carbonous substrate, as confirmed from the TEM images.

197　　The SSA and PV of MmBCs were given in Fig. 1a. SSA dramatically decreased from

198 174.1 to 45.8~52.8 m^2 g^{-1} and PV decreased from 40.0 to 10.5~12.1 cm^3 g^{-1}after

199 magnetite introduction. These values are much lower than those of pristine ball milled

200 biochar base and even slightly lower than the parameters of the magnetite (SSA and PV

201 are 71.3 m^2 g^{-1} and 16.4 cm^3 g^{-1}, respectively), implying that the clogging and

202 agglomeration of micro- and meso-pores on the adsorbent takes place. Although this

203 depressed phenomenon has already been reported, the decline ratios of the SSA and PV

204 in this work were much lower than those in literatures (Li et al., 2020b; Wang et al.,

205 2020a), which should be beneficial from the ultrafine magnetite.

206　　The decreased functional groups as well as SSA and PV are expected to reduce the

207 active sites for contaminant adsorption and lead to decreased capacity. As observed in

208 Fig. 1b, the removal capacity of MmBCs to MB reduced 1.75-2 times after deposition.

209 As calculated from the precursors, the magnetite amount in the raw material of MmBC-

210 0.6 was no more than ~28 wt%. Considering that the magnetite takes 28 wt% of the

211 adsorbent and was found to have a quite low capacity of only 0.738±0.096 mg g^{-1}, the

212 capacity of MmBC-0.6 was calculated to reduce 1.4 times, which is lower than the

213 actual value. Therefore, the diminished adsorption performance should be influenced

214 by not only the magnetite itself, but also the decreased functional groups as well as SSA

215 and PV after deposition. As MmBC-0.6 has the best adsorption performance with

216 acceptable magnetism, it was applied for the following experiments unless otherwise

217 mentioned.

218 **3.2 The second ball milling for adsorption recovery**

219 Mechanical milling is considered an effective way to functionalize the surface and

220 improve the capacity of adsorbents (Kumar et al., 2020). Therefore, a second ball

221 milling step was carried out to re-activate the adsorbent at various rotating speeds.

222 There were no structural and compositional changes and there was no magnetic loss

223 after due to the second milling step as indicated by XRD and magnetic hysteresis loops,

224 implying that the composite adsorbent was not damaged. Therefore, the resulting

225 magnetic biochar is expected to keep its magnetism, also after reutilization.

226 Microscopic images also confirmed the maintained structure of the composites. The

227 magnetic nanoparticles were in close contact with the biochar even after strong

228 mechanical milling. Their dispersion was also not affected (see supplementary

229 materials).

230 However, the size of the adsorbents was slightly reduced to ~261.9-284.5 nm due to

231 the high energy shear forces. FT-IR spectra indicated a qualitative recovery of C=C and

232 –OH vibration groups, which was in agreement with the titration results. As shown by

233 titration (Table 1), the carboxyl, lactonic and phenolic groups of MmBC-BMs were

234   gradually recovered and reached a level of >93.7% of the corresponding groups of ball

235   milled biochar while the recovery rate for the total acidic groups was up to 97.3%.

236   Increases in aromaticity (C=C) as well as in O-containing functional groups have also

237   been reported for ball milled biochar (Xiang et al., 2020) as biochar can be oxidized

238   with air in the jar and created with chemical bonds through the promoted solid phase

239   reactions with generated heat and kinetic energy from ball milling process (Li et al.,

240   2020b; Rojas-Chavez et al., 2009). With the recovery of the surface functional groups,

241   zeta potentials of the adsorbent were also recovered to some degree.

242   The SSA and PV of the resultant samples also remarkably recovered with milling, a

243   recovery in which the rotation speed played an important role. As shown in Fig. 1c, the

244   SSA and PV increased from 52.0 to 67.3, 104.5, 112.8, 139.2 m^2 g^{-1} and 11.9 to 15.5,

245   24.0, 25.9, 32.0 cm^3 g^{-1} with 100, 200, 300 and 400 rpm, respectively. The SSA and PV

246   of the magnetite after milling on the other hand surprisingly decreased to 31.3 m^2 g^{-1}

247   and 7.2 cm^3 g^{-1}. Therefore, a collapse of the pore network in magnetite is apparent. As

248   discussed before, the magnetite amount in the raw material of MmBC-0.6 was no more

249   than ~28 wt%. That means the ball-milled biochar-based SSA and PV for MmBC-

250   BM400 are calculated to be 181.2 m^2 g^{-1} and 41.6 cm^3 g^{-1} by deducting the SSA and

251   PV induced by 28 wt% magnetite. In fact, the presented magnetite should be lower than

252   the theoretical value of 28% as the Fe precursor may not completely transform to

253   magnetite. Thus, the actual SSA and PV for the ball-milled biochar base may be slightly

254   lower than the calculated value of 181.2 m^2 g^{-1} and 41.6 cm^3 g^{-1}. Nevertheless, it is

255   undisputable that the actual SSA and PV values are close to those of the pristine ball

milled biochar without magnetite loading. As ball milling is usually accompanied by crystal deformation and defect appearance (Uzarevic et al., 2015; Zhuang et al., 2016), it is speculated that the clogging of the pores was partially undone and that some new pores as well as new defects were generated in biochar with the shearing force from the co-milled hard and ultrafine magnetite (Yang et al., 2020).

Benefitting from the recovered O-containing functional groups as well as SSA and PV, the adsorption performance was also recovered and reached a higher adsorption capacity of 84.6±2.5 mg/L. As shown in Fig. 1d, q_e for the specific sample recovered to 60.9, 68.4, 84.5 and 93.8% of the capacity of the pristine ball milled biochar as the rotation speed reached to 100, 200, 300 and 400 rpm respectively. The capacity of the ball milled magnetite was 0.846±0.024 mg g^{-1}, nearly the same as that before milling. Therefore, the physicochemical changes of biochar platform played a dominant role in its recovery.

To evaluate the adsorption efficiency, the MmBC-MB400 was also compared with magnetic biochar fabricated with two pathways. Guided by Li, impregnated magnetic biochar (i-MBCs) was first prepared with impregnation and pyrolysis with FeCl$_3$ followed by ball milling (Li et al., 2020a, see supplementary materials). FT-IR and XRD patterns confirmed the successful introduction of magnetite. The size and zeta potential of the samples were influenced by the FeCl$_3$ concentration, implying that the amount of magnetite loaded increased with increasing magnetite concentrations. However, the adsorption capacities of i-MBCs declined with concentration, and were much lower than those of MmBC-BMs. In a 2nd pathway, biochar was utilized directly without any

278 pretreatment. After magnetite deposition, the composites were ball milled. FT-IR and

279 XRD patterns confirmed the successful introduction of magnetite with intensified

280 characteristic peaks *versus* an increased the mass ratio between Fe(acac)$_3$ and biochar.

281 These as-obtained magnetic biochar (MBCs) had a slightly larger size and higher zeta

282 potentials (see supplementary materials). However, their adsorption capacities were

283 lower than those of MmBC-BMs. Therefore, an optimized magnetic biochar was

284 needed and developed in the present work, in which the extra ball milling greatly

285 promoted its capacity for adsorption.

286 The SSA and adsorption capacity of MmBC-BM400 on MB were also compared

287 with those of magnetic biochar in literatures (see supplementary materials). A decrease

288 in SSA was observed in all of the magnetic biochar, implying the commonly existence

289 of pore blockage. However, through second ball milling process, the SSA was largely

290 recovered in this work, resulting in a comparable adsorption capacity with pristine ball

291 milled biochar. Notably, the adsorption capacity of MmBC-BM400 is not as

292 outstanding as some other adsorbents in the literature, which should be ascribed to the

293 rather limited SSA of 174.1 m^2 g^{-1} and the MB removal capacity of 90.2 mg g^{-1} for the

294 pristine ball milled biochar. It is therefore reasonable to expect that the adsorption of

295 the material as developed here can be further improved by optimizing raw material as

296 well as the carbonizations (Lyu et al., 2018; Park et al., 2019). Thus, an innovative,

297 efficient and highly controllable strategy was provided for preparing high-performance

298 and recoverable biochar-based magnetic adsorbents, which are environmentally

299 friendly and economically favorable for decontamination of aqueous organic wastes.

3.3 Studies of adsorption kinetics, isotherms and thermodynamics

As depicted in Fig. 2a, the adsorption of MmBC-BM400 is a function of the length of the adsorption period. A fast adsorption stage was observed in the initial 6 h, in which 82.5% MB were adsorbed. After that, the adsorption became much slower and equilibrium was finally achieved after 24 h. To evaluate the adsorption mechanism of the adsorbent, pseudo-first-order and pseudo-second-order kinetic models were applied (Qi et al., 2022). The results are presented in Fig. 2b, c and Table 2. More similar q_e and higher R^2 (0.997) was observed with the pseudo-second-order model. Therefore, the adsorption of MB onto MmBC-BM400 is proposed to be a chemisorption-dominated process, because the pseudo-second-order model describes the adsorption process better (Zhou et al., 2022).

An intra-particle diffusion model was further utilized to evaluate the rate limiting step(s) of the sorption process. As indicated in Fig. 2d and Table 2, two parts of linear relationship with different slopes and intercepts were obtained by curve fitting, indicating a two-stage rate limiting steps in this system. k_{d2} is much lower than k_{d1}, representing a much higher adsorption rate at the first stage. This is reasonable as the nanocomposite has ample active sites on the surface for MB adsorption in the initial stage. In this stage, external diffusion takes place with MB molecules transferred from the bulk solution to the surface of the adsorbent. Over time active sites on the surface were gradually occupied and adsorption slowed down as it was controlled by internal diffusion to the abundantly present micro- and meso-pores (Liu et al., 2021). However,

321 both the C_i are non-zero, indicating the adsorption mechanism is quite complex, and

322 may not only be controlled by intra-particle diffusion (Yamaguchi et al., 2016).

323   The adsorption isotherms were further studied to describe the interactive behaviors

324 between adsorbate and asorbent. The adsorption was better fitted with Freundlich

325 (R^2=0.994) than Langmuir isotherm models (R^2=0.980), implying the adsorption was

326 heterogeneous and controlled by multiple mechanisms (Fig. 2e and Table 3) (Lyu et al.,

327 2018).

328   To determine the thermodynamic parameters including entropy change ($\Delta S°$, J mol^{-1}

329 K^{-1}), enthalpy change ($\Delta H°$, kJ mol^{-1}) and standard Gibbs free energy change ($\Delta G°$, kJ

330 mol^{-1}) of MB adsorption onto MmBC-BM400, adsorption were conducted at five

331 different temperatures from 25 to 60 °C. lnK_d *versus* 1/T is plotted in Fig. 2f and the

332 parameters were listed in Table 4. The negative $\Delta G°$ decreased with the temperature,

333 indicating the spontaneous nature of the adsorption. The positive $\Delta H°$ suggests the

334 adsorption is an endothermic process and the capacity increases with the temperature

335 within 25-60 °C. The positive value of $\Delta S°$ indicates an increased randomness at the

336 adsorbate-adsorbent interfaces during the adsorption progress (Khan et al., 2012).

337 **3.4 Possible adsorption mechanisms**

338   Both MmBC-0.6 and MmBC-BM400 were negatively charged while MB is cationic

339 in aqueous solutions (see supplementary materials). Therefore, electrostatic interaction

340 is likely one of the driving forces for adsorption (Wang et al., 2019). To illustrate these

341 interactions, the adsorption performance and the zeta potentials of MmBC-0.6 and

342 MmBC-BM400 with regulated solution pH were measured (Fig. 3a). The capacity was

16

343 increased when the solution pH increased. As the points of zero charge of MmBC-0.6

344 and MmBC-BM400 are both around 4.0, at the solution pH>4.0, acidic functional

345 groups, as evidenced in FT-IR and boehm's titration, are deprotonated. Electrostatic

346 interactions between the MB and the adsorbent gradually developed and strengthened,

347 thus greatly improving the adsorption performance. However, at solution pH<4.0,

348 surface functional groups are protonated, leading to electrostatic repulsion with cationic

349 MB and correspondingly diminished adsorption performance. However, MmBC-0.6

350 and MmBC-BM400 still showed an adsorption capacity over 20 and 60 mg g^{-1} for MB

351 at pH<4.0. Meanwhile, kinetics and isotherms of MmBC-BM400 also implied the

352 adsorption was quite complex and dominated by chemisorption. Therefore, the

353 adsorption was also driven by other interactions.

354   To further determine the possible adsorption mechanism, FT-IR spectra of the

355 MmBC-0.6 and MmBC-BM400 before and after adsorption were also depicted (see

356 supplementary materials). As discussed before, the recovery of C=C and –OH vibration

357 after milling was confirmed by both FT-IR spectra and the titration result (Table 1),

358 leading to increased aromaticity (C=C) as well as O-containing functional groups.

359 However, the peaks of aromatic C=C become sharper after adsorption and the peaks of

360 phenolic –OH at 1402 cm^{-1} also changed while MB belonged –CH$_3$ peak at 1323 cm^{-1}

361 was newly formed in both MmBC-0.6 and MmBC-BM400 samples. This implies that

362 the MB molecules interacted with the adsorbents through these unsaturated bonds

363 (Munkhbayar et al., 2013). Especially, the aromaticity (C=C bond) is expected to

364 promote the adsorption via π-π interactions (Alchouron et al., 2021). The increase of

365   O-containing groups is also likely to enhance MB adsorption via ion exchange

366   mechanism (Li et al., 2018). Meanwhile, the –N(CH$_3$)$_2$ in MB molecules could serve

367   as H$^+$ acceptors while –OH on MmBC-BM400 served as H$^+$ donors. Therefore,

368   hydrogen bonding was also believed as one of the driving forces for adsorption.

369   Although the adsorption of magnetic biochar before and after milling was driven by

370   multiple interactions (illustrated in Fig. 4), their differences should be originated from

371   the physicochemical properties of the adsorbents as discussed above. MmBC-0.6 and

372   MmBC-BM400 share similar zeta potentials in water, however the adsorption of

373   MmBC-0.6 was much lower than that of MmBC-BM400 at the point of zero charge,

374   indicating the interactions except electrostatic force as well as the difference in SSA

375   and PV played a significant role in adsorption. Similarly, it is noted that the biochar ball

376   milled at 300 rpm and 400 rpm for 5 h have similar zeta potentials in water, indicating

377   the electrostatic interactions were almost identical. However, these kinds of biochar

378   have different SSA and PV. Therefore, the similarity in their adsorption capacities

379   should be ascribed to their similar functional groups for π-π, hydrogen interacted and/or

380   ion exchanged with MB. That means the surface functional groups played a major role

381   in the adsorption. For MmBC-0.6 and MmBC-BM400, the surface functional groups

382   and the aromaticity (C=C bond) of the latter was recovered and increased, leading to

383   increased ion exchange, π-π and hydrogen interactions than the former one. At the same

384   time, the SSA and PV were recovered by breaking the enfolding of the pores and

385   generating new pores in biochar with the shearing force from the co-milled hard and

386   ultrafine magnetite, thus also providing some additional sites for adsorption. Therefore,

387   the MmBC-BM400 shows a pronounced recovered capacity.

388   **3.5 Regeneration and recyclability of the adsorbent**

389   The recyclability of MmBC-BM400 was examined with ethanol as sorbate. As

390   shown in Fig. 3b, the capacity was only slightly decreased after four cycles, indicating

391   a maintained adsorption performance of the adsorbent after usage. The observed

392   reduction in performance was attributed to a loss of adsorption sites due to strongly

393   attached or trapped MB molecules on the surface of the biochar or within the pores.

394   Residual non-desorbed ethanol molecules may further have contributed to the reduction

395   in adsorption performance (Cho et al., 2016).

396   **4. Conclusion**

397   An optimized magnetic biochar was developed with both excellent sorption and re-

398   use characteristics. This material was produced by impregnating ball-milled biochar

399   with magnetite followed by an extra ball milling step to counteract the reduction in

400   adsorption invariably caused by magnetite loading. Following the extra milling step the

401   magnetic biochar exhibited a decrease in adsorption relative to non-magnetic ball-

402   milled biochar of only 6.2%. The restoration of SSA and surface functional groups

403   played a vital role in the recovery. The simple ball milling step is also regarded as an

404   effective way for adsorption recovery of pore-clogged adsorbents loaded with

405   functional nanoparticles.

406   **CRediT authorship contribution statement**

407   **Nina Yan:** Conceptualization, Methodology, Writing – review & editing, Funding

408   acquisition. **Biao Hu:** Data curation, Writing – original draft. **Zhiyu Zheng:** Data

409   curation, Methodology. **Haiying Lu:** Writing – review & editing, Funding acquisition.

410   **Jingwen Chen:** Data curation. **Xiaomei Zhang:** Data curation. **Xizhi Jiang:**

411   Methodology. **Yonghong Wu**: Writing – review & editing. **Jan Dolfing**: Writing –

412   review & editing. **Lei Xu:** Supervision, Funding acquisition.

413   **Declaration of Competing Interest**

414   The authors declare that they have no known competing financial interests or

415   personal relationships that could have appeared to influence the work reported in this

416   paper.

417   **Data availability**

418   Data will be made available on request.

425   **Appendix A. Supplementary data**

426   E-supplementary data for this work can be found in e-version of this paper online.

427

References

1. Alchouron, J., Navarathna, C., Rodrigo, P. M., Snyder, A., Chludil, H. D., Vega, A. S., Bosi, G., Perez, F., Mohan, D., Pittman, C. U., Mlsna, T. E., 2021. Household arsenic contaminated water treatment employing iron oxide/ bamboo biochar composite: An approach to technology transfer. J. Colloid Interface Sci. 587, 767-779.

2. Boehm, H. P., 1994. Some aspects of the surface-chemistry of carbon-blacks and other carbons. Carbon 32, 759-769.

3. Cai, W., Wan, J. Q., 2007. Facile synthesis of superparamagnetic magnetite nanoparticles in liquid polyols. J. Colloid Interface Sci. 305, 366-370.

4. Cao, L. D., Ma, D. K., Zhou, Z. L., Xu, C. L., Cao, C., Zhao, P. Y., Huang, Q. L., 2019. Efficient photocatalytic degradation of herbicide glyphosate in water by magnetically separable and recyclable BiOBr/Fe3O4 nanocomposites under visible light irradiation. Chem. Eng. J. 368, 212-222.

5. Cho, D. W., Lee, J., Ok, Y. S., Kwon, E. E., Song, H., 2016. Fabrication of a novel magnetic carbon nanocomposite adsorbent via pyrolysis of sugar. Chemosphere 163, 305-312.

6. Dollimore, D.; Spooner, P.; Turner, A, 1976. The bet method of analysis of gas adsorption data and its relevance to the calculation of surface areas. Surf. Technol. 4, 121‑160.

7. El-Naggar, A. L., Mosa, A., Ahmed, N., Niazi, N. K., Yousaf, B., Sarkar, B., Rinklebe, J., Cai, Y. J., Chang, S. X., 2022. Modified and pristine biochars for

450   remediation of chromium contamination in soil and aquatic systems. Chemosphere

451   303, 134942.

452   8. Huang, Z. X., Yi, Y. Q., Zhang, N. Q., Tsang, P. E., Fang, Z. Q., 2022. Removal of

453   fluconazole from aqueous solution by magnetic biochar treated by ball milling:

454   adsorption performance and mechanism. Environ. Sci. Pollut. Res. 29, 33335-

455   33344.

456   9. Khan, T. A., Dahiya, S., Ali, I., 2012. Use of kaolinite as adsorbent: Equilibrium,

457   dynamics and thermodynamic studies on the adsorption of Rhodamine B from

458   aqueous solution. Appl. Clay Sci. 69, 58-66.

459 10. Kumar, M., Xiong, X. N., Wan, Z. H., Sun, Y. Q., Tsang, D. C. W., Gupta, J., Gao,

460   B., Cao, X. D., Tang, J. C., Ok, Y. S., 2020. Ball milling as a mechanochemical

461   technology for fabrication of novel biochar nanomaterials. Bioresour. Technol. 312,

462   123613.

463 11. Li, M. R., Wei, D., Liu, T., Liu, Y. R., Yan, L. G., Wei, Q., Du, B., Xu, W. Y., 2019.

464   EDTA functionalized magnetic biochar for Pb(II) removal: Adsorption performance,

465   mechanism and SVM model prediction. Sep. Purif. Technol. 227, 115696.

466 12. Li, R. H., Zhang, Y. C., Deng, H. X., Zhang, Z. Q., Wang, J. J., Shaheen, S. M.,

467   Xiao, R., Rinklebe, J., Xi, B. D., He, X. S., Du, J., 2020a. Removing tetracycline

468   and Hg(II) with ball-milled magnetic nanobiochar and its potential on polluted

469   irrigation water reclamation. J. Hazard. Mater. 384, 121095.

470 13. Li, Y. F., Liu, X., Zhang, P. Z., Wang, X. L., Cao, Y. Y., Han, L. J., 2018. Qualitative

471   and quantitative correlation of physicochemical characteristics and lead sorption

22

472   behaviors of crop residue-derived chars. Bioresour. Technol. 270, 545-553.

473   14. Li, Y. F., Zimmerman, A. R., He, F., Chen, J. J., Han, L. J., Chen, H., Hu, X., Gao,

474   B., 2020b. Solvent-free synthesis of magnetic biochar and activated carbon through

475   ball-mill extrusion with Fe3O4 nanoparticles for enhancing adsorption of

476   methylene blue. Sci. Total Environ. 722, 137972.

477   15. Liu, H. D., Xu, G. R., Li, G. B., 2021. Preparation of porous biochar based on

478   pharmaceutical sludge activated by NaOH and its application in the adsorption of

479   tetracycline. J. Colloid Interface Sci. 587, 271-278.

480   16. Lyu, H. H., Gao, B., He, F., Zimmerman, A. R., Ding, C., Tang, J. C., Crittenden, J.

481   C., 2018. Experimental and modeling investigations of ball-milled biochar for the

482   removal of aqueous methylene blue. Chem. Eng. J. 335, 110-119.

483   17. Munkhbayar, B., Nine, M. J., Jeoun, J., Bat-Erdene, M., Chung, H., Jeong, H., 2013.

484   Influence of dry and wet ball milling on dispersion characteristics of the multi-

485   walled carbon nanotubes in aqueous solution with and without surfactant. Powder

486   Technol. 234, 132-140.

487   18. Park, J. H., Wang, J. J., Kim, S. H., Kang, S. W., Jeong, C. Y., Jeon, J. R., Park, K.

488   H., Cho, J. S., Delaune, R. D., Seo, D. C., 2019. Cadmium adsorption characteristics

489   of biochars derived using various pine tree residues and pyrolysis temperatures. J.

490   Colloid Interface Sci. 553, 298-307.

491   19. Qi, G. D., Pan, Z. F., Zhang, X. Y., Miao, X. D., Xiang, W., Gao, B., 2022. Effect

492   of ball milling with hydrogen peroxide or ammonia hydroxide on sorption

490   performance of volatile organic compounds by biochar from different pyrolysis

494   temperatures. Chem. Eng. J. 450, 138027.

495 20. Qu, J. H., Wu, Z. H., Liu, Y., Li, R. L., Wang, D., Wang, S. Q., Wei, S. Q., Zhang,

496   J. R., Tao, Y., Jiang, Z., Zhang, Y., 2022. Ball milling potassium ferrate activated

497   biochar for efficient chromium and tetracycline decontamination: Insights into

498   activation and adsorption mechanisms. Bioresour. Technol. 360, 127407.

499 21. Rojas-Chavez, H., Diaz-de la Torre, S., Jaramillo-Vigueras, D., Plascencia, G., 2009.

500   PbTe mechanosynthesis from PbO and Te. J. Alloy. Compd. 483, 275-278.

501 22. Shan, D. N., Deng, S. B., Zhao, T. N., Wang, B., Wang, Y. J., Huang, J., Yu, G.,

502   Winglee, J., Wiesner, M. R., 2016. Preparation of ultrafine magnetic biochar and

503   activated carbon for pharmaceutical adsorption and subsequent degradation by ball

504   milling. J. Hazard. Mater. 305, 156-163.

505 23. Shang, J. G., Pi, J. C., Zong, M. Z., Wang, Y. R., Li, W. H., Liao, Q. H., 2016.

506   Chromium removal using magnetic biochar derived from herb-residue. J. Taiwan

507   Inst. Chem. Eng. 68, 289-294.

508 24. Son, E. B., Poo, K. M., Chang, J. S., Chae, K. J., 2018. Heavy metal removal from

509   aqueous solutions using engineered magnetic biochars derived from waste marine

510   macro-algal biomass. Sci. Total Environ. 615, 161-168.

511 25. Tang, J. Y., Ma, Y. F., Cui, S., Ding, Y. Z., Zhu, J. Y., Chen, X., Zhang, Z. L., 2022.

512   Insights on ball milling enhanced iron magnesium layered double oxides bagasse

513   biochar composite for ciprofloxacin adsorptive removal from water. Bioresour.

514   Technol. 359, 127468.

515   26. Uzarevic, K., Halasz, I., Friscic, T., 2015. Real-Time and In Situ Monitoring of

516   Mechanochemical Reactions: A New Playground for All Chemists. J. Phys. Chem.

517   Lett. 6, 4129-4140.

518   27. Wang, B., Zhai, Y. B., Wang, T. F., Li, S. H., Peng, C., Wang, Z. X., Li, C. T., Xu,

519   B. B., 2019. Fabrication of bean dreg-derived carbon with high adsorption for

520   methylene blue: Effect of hydrothermal pretreatment and pyrolysis process.

521   Bioresour. Technol. 274, 525-532.

522   28. Wang, K., Sun, Y. B., Tang, J. C., He, J., Sun, H. W., 2020a. Aqueous Cr(VI)

523   removal by a novel ball milled Fe-0-biochar composite: Role of biochar electron

524   transfer capacity under high pyrolysis temperature. Chemosphere 241, 125044.

525   29. Wang, X. D., Xu, J., Liu, J., Liu, J., Xia, F., Wang, C. C., Dahlgren, R. A., Liu, W.,

526   2020b. Mechanism of Cr(VI) removal by magnetic greigite/biochar composites.

527   Sci. Total Environ. 700, 134414.

528   30. Xiang, W., Wan, Y. S., Zhang, X. Y., Tan, Z. Z., Xia, T. T., Zheng, Y. L., Gao, B.,

529   2020a. Adsorption of tetracycline hydrochloride onto ball-milled biochar:

530   Governing factors and mechanisms. Chemosphere 255, 127057.

531   31. Xiang, W., Zhang, X. Y., Chen, K. Q., Fang, J. N., He, F., Hu, X., Tsang, D. C. W.,

532   Ok, Y. S., Gao, B., 2020b. Enhanced adsorption performance and governing

533   mechanisms of ball-milled biochar for the removal of volatile organic compounds

534   (VOCs). Chem. Eng. J. 385, 123842.

535   32. Yamaguchi, N. U., Bergamasco, R., Hamoudi, S., 2016. Magnetic MnFe2O4-

536   graphene hybrid composite for efficient removal of glyphosate from water. Chem.

537   Eng. J. 295, 391-402.

538   33. Yang, X., Yu, I. K. M., Tsang, D. C. W., Budarin, V. L., Clark, J. H., Wu, K. C. W.,

539   Yip, A. C. K., Gao, B., Lam, S. S., Ok, Y. S., 2020. Ball-milled, solvent-free Sn-

540   functionalisation of wood waste biochar for sugar conversion in food waste

541   valorisation. J. Clean Prod. 268, 122300.

542   34. Zeng, H. P., Qi, W., Zhai, L. X., Wang, F. S., Zhang, J., Li, D., 2021. Preparation

543   and characterization of sludge-based magnetic biochar by pyrolysis for methylene

544   blue removal., Nanomaterials 11, 2473.

545   35. Zhang, P., O'Connor, D., Wang, Y. N., Jiang, L., Xia, T. X., Wang, L. W., Tsang, D.

546   C. W., Ok, Y. S., Hou, D. Y., 2020. A green biochar/iron oxide composite for

547   methylene blue removal. J. Hazard. Mater. 384, 121286.

548   36. Zheng, Z. Y., Chen, J. W., Wu, J. M., Feng, M., Xu, L., Yan, N. N., Xie, H. D., 2021.

549   Incorporation of biomass-based carbon nanoparticles into polysulfone

550   ultrafiltration membranes for enhanced separation and anti-fouling performance.

551   Nanomaterials 11, 2303.

552   37. Zhou, L., Chi, T.Y., Zhou, Y.Y., Lv, J.D., Chen, H., Sun, S.Q., Zhu, X.F., Wu, H.P.,

553   Hu, X., 2022. Efficient removal of hexavalent chromium through adsorption-

554   reduction-adsorption pathway by iron-clay biochar composite prepared from

555   Populus nigra. Sep. Purif. Technol. 285, 120386.

556   38. Zhuang, S. Q., Lee, E. S., Lei, L., Nunna, B. B., Kuang, L. Y., Zhang, W., 2016.

557   Synthesis of nitrogen-doped graphene catalyst by high-energy wet ball milling for

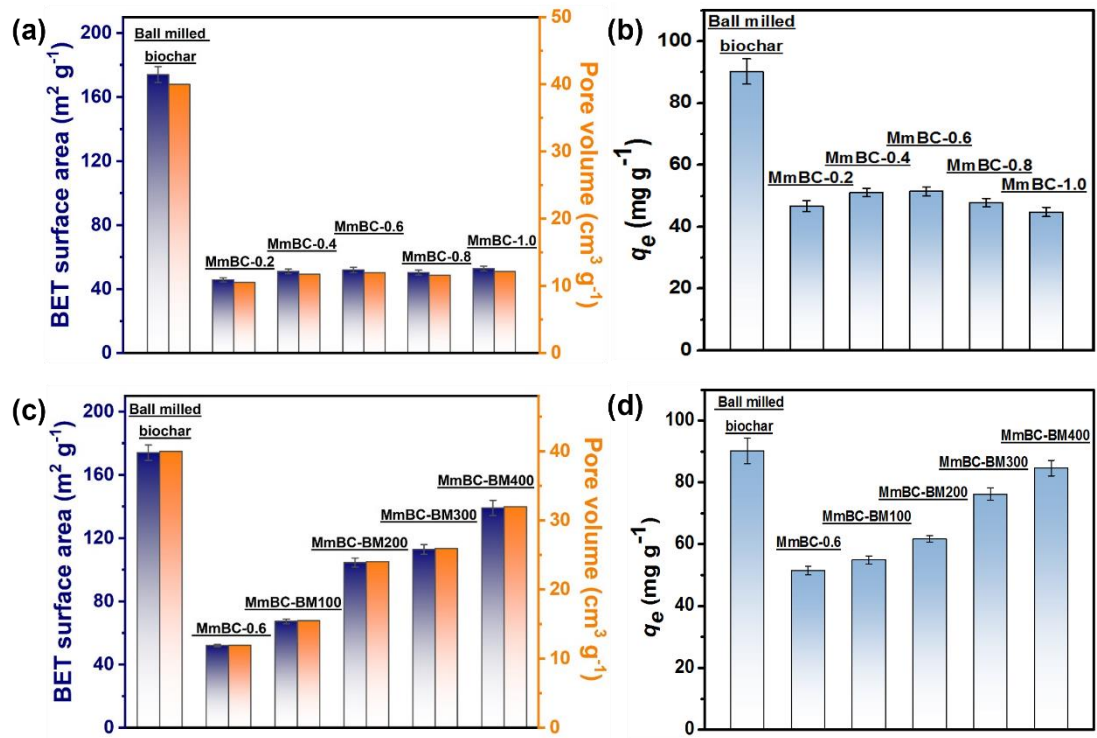558   electrochemical systems. Int. J. Energy Res. 40, 2136-2149.
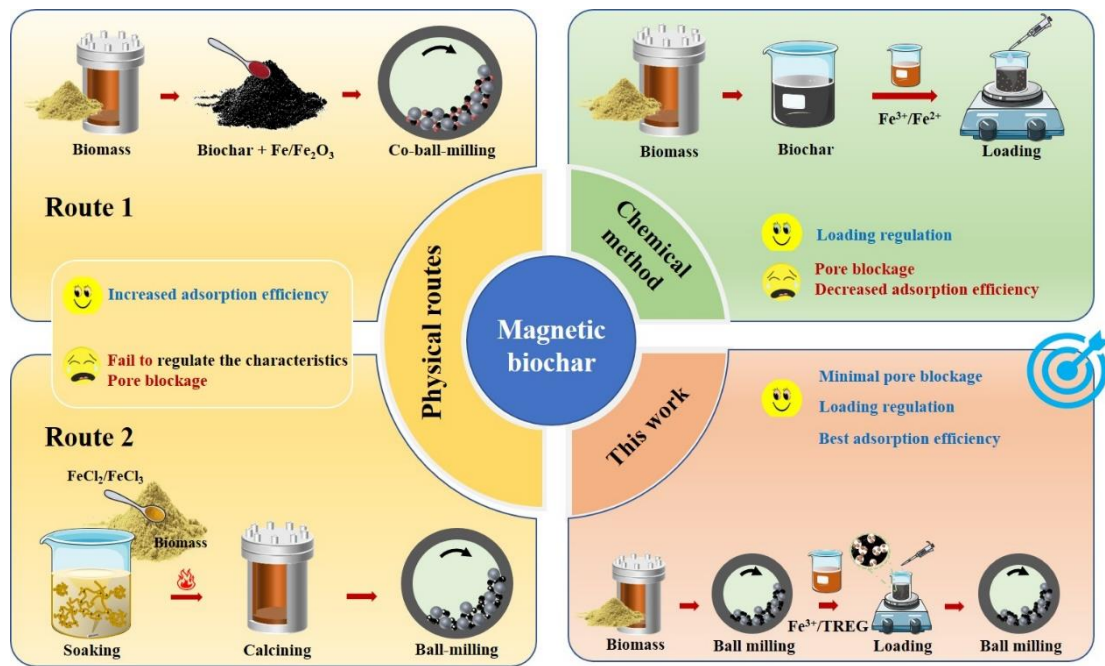
559

560 **Scheme 1.** Comparison between the traditional methods and this work for preparation
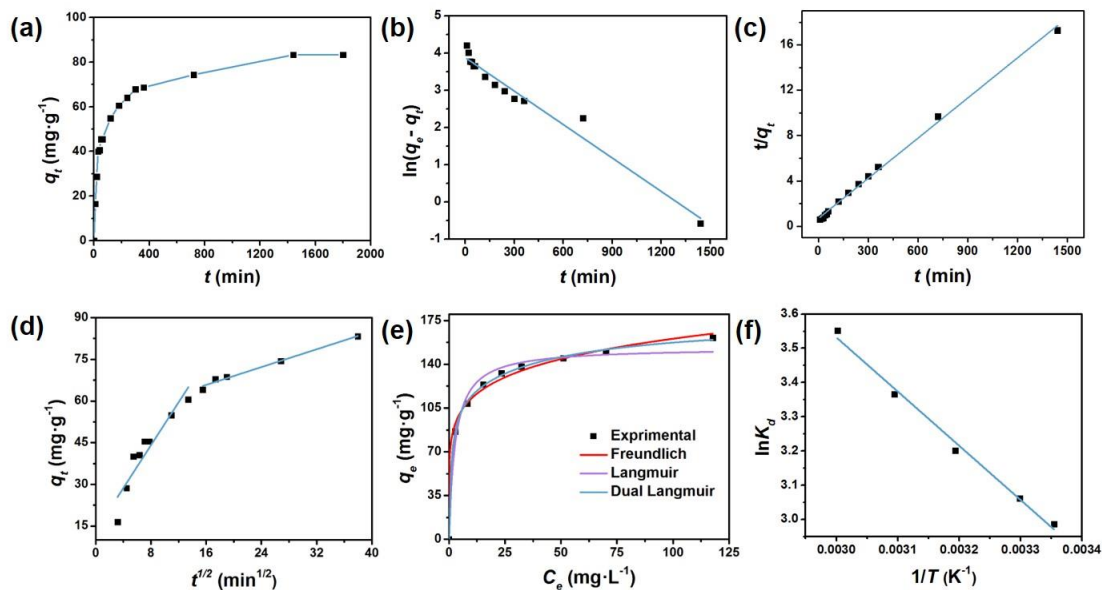
561 of magnetic biochar.

562

Fig. 1. (a) BET and (b) q_e of ball milled biochar and MmBCs, respectively; (c) BET and (d) q_e of ball milled biochar, MmBC-0.6 and MmBC-BMs, respectively.

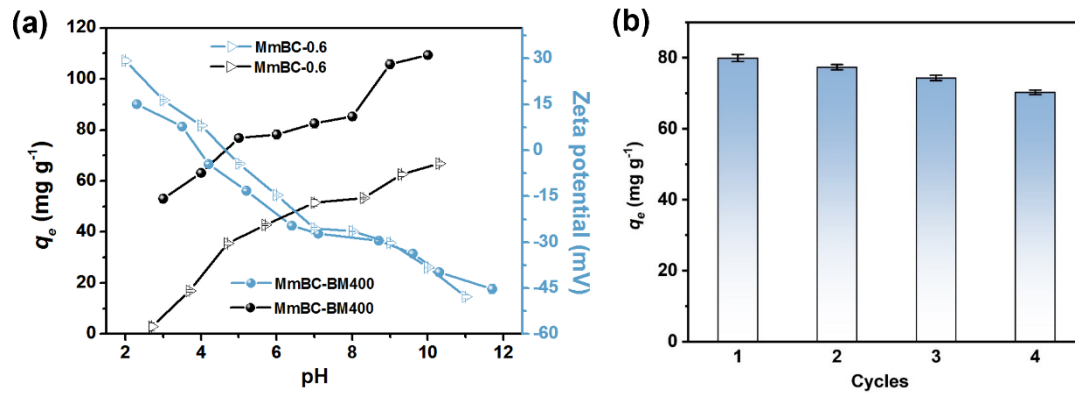**Fig. 2.** MB adsorption kinetics, isotherms and thermodynamics on MmBC-BM400. (a) The experimental adsorption, (b) pseudo-first-order, (c) pseudo-second-order and (d) intra-particle diffusion models of MmBC-BM400 for MB adsorption. (e) Isotherm models fitting for MB adsorption on MmBC-BM400 at 25 °C. (f) $\ln K_d$ versus $1/T$ for adsorption of MB on MmBC-BM400 at various temperatures.
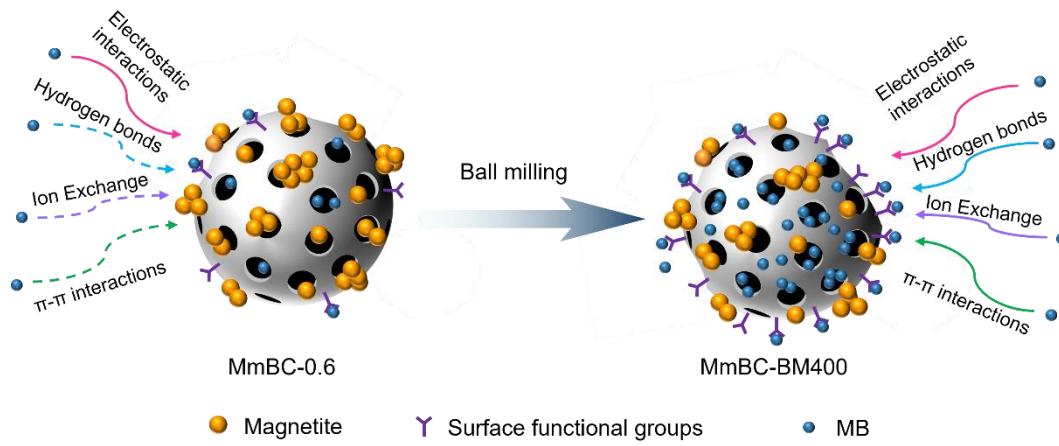
574

Fig. 3. (a) Effect of solution pH on MB adsorption onto MmBC-0.6 and MmBC-BM400
and the zeta potential of the two adsorbents; (b) adsorption capacity of MmBC-BM400
for different reutilization times.

579

580   **Fig. 4.** Adsorption mechanism of magnetic biochar before and after second ball milling.

581

582 **Table 1.** Surface functional groups of different samples in this study

Sample	Total acidic groups (mmol g^{-1})	Carboxyl (mmol g^{-1})	Lactonic (mmol g^{-1})	Phenolic hydroxyl (mmol g^{-1})
Biochar	0.173	0.066	0.009	0.098
Magnetite	0.106	0.028	0.037	0.041
Ball milled biochar	0.598	0.207	0.026	0.365
MmBC-0.6	0.271	0.094	0.019	0.158
MmBC-BM100	0.378	0.119	0.020	0.239
MmBC-BM200	0.438	0.179	0.020	0.239
MmBC-BM300	0.537	0.199	0.025	0.313
MmBC-BM400	0.582	0.194	0.028	0.360

583

584

585 **Table 2.** Kinetic parameters for different adsorption models in this study

Kinetic models	Parameters	MmBC-BM400
Experimental	q_e (mg g^{-1})	84.6
Pseudo-first-order	q_e(mg g^{-1})	48.4
	k_1(min^{-1})	0.003
	R^2	0.963
Pseudo-second-order	q_e (mg g^{-1})	84.6
	k_2 (g mg^{-1} min^{-1})×10^{-4}	2.064
	R^2	0.997
Intra-particle diffusion	k_{d1} (mg g^{-1} min$^{-0.5}$)	3.854
	C_1 (mg g^{-1})	13.261
	R_1^2	0.852
	k_{d2} (mg g^{-1} min$^{-0.5}$)	0.802
	C_2 (mg g^{-1})	52.979
	R_2^2	0.982

586

587

588 **Table 3.** Parameters of adsorption isotherm models in this study

Isotherm models	Parameters	Values
Langmuir	q_L (mg g^{-1})	153.5
	k_L (L mg^{-1})	0.363
	R^2	0.980
Freundlich	n	6.495
	k_F ((mg g^{-1})(L mg^{-1})$^{1/n}$)	78.96
	R^2	0.994

589

590

591   **Table 4.** Thermodynamic parameters of MB adsorption on MmBC-BM400

T (K)	K_d (L g^{-1})	$\Delta G^\bullet$ (kJ mol^{-1})	$\Delta H^\bullet$ (kJ mol^{-1})	$\Delta S^\bullet$ (J mol^{-1} K^{-1})
298.15	19.81	-7.36		
303.15	21.35	-7.71		
313.15	24.56	-8.40	13.17	68.87
323.15	28.94	-9.09		
333.15	34.88	-9.78		

592
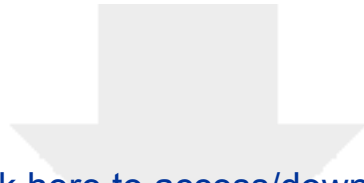
Click here to access/download
Electronic Annex
Supporting information-revised.docx